

A Hypertoroidal Covering for Perfect Color Equivariance

Yulong Yang^{1,*} Zhikun Xu^{1,2,*} Yaojun Li¹ Christine Allen-Blanchette^{1,†}
¹Princeton University, USA ² Tsinghua University, China
 {yulong.yang, zx7925, y13425, ca15}@princeton.edu

Abstract

When the color distribution of input images changes at inference, the performance of conventional neural network architectures drops considerably. A few researchers have begun to incorporate prior knowledge of color geometry in neural network design. These color equivariant architectures have modeled hue variation with 2D rotations, and saturation and luminance transformations as 1D translations. While this approach improves neural network robustness to color variations in a number of contexts, we find that approximating saturation and luminance (interval valued quantities) as 1D translations introduces appreciable artifacts. In this paper, we introduce a color equivariant architecture that is truly equivariant. Instead of approximating the interval with the real line, we lift values on the interval to values on the circle (a double-cover) and build equivariant representations there. Our approach resolves the approximation artifacts of previous methods, improves interpretability and generalizability, and achieves better predictive performance than conventional and equivariant baselines on tasks such as fine-grained classification and medical imaging tasks. Going beyond the context of color, we show that our proposed lifting can also extend to geometric transformations such as scale.

1 Introduction

While shape and geometry dominate human object perception, color information plays an increasing role for more fine grained visual tasks (Bramão et al., 2011). However, until recently (Lengyel et al., 2021, 2023; Yang et al., 2024), principled design based on perceptual information has attracted less attention when designing networks even though its empirical importance for performance was noted early on (Engilberge et al., 2017).

A popular early heuristic for dealing with perceptual variations is to simply transform the images to gray scale (Günes et al., 2016; Xie & Richmond, 2018). However, the assumption that the training and testing images are drawn from the same distribution limits the generalizability of these models. Data augmentation techniques (Hendrycks et al., 2019, 2021) seek to find a systematic way to expand the training dataset to capture more variations, but at the expense of increased training time and computation resources. Color invariant networks (Lengyel et al., 2021) leverage the geometric structure of color to ensure that perceptual variations do not affect network outputs. This however discards important information that is especially valuable on tasks such as fine-grained classification. Color equivariant approaches allow the network to retain color information by leveraging the geometric structure of color. However, existing techniques are only able to be approximately equivariant to only the hue channel (Lengyel et al., 2023) or exhibits artifacts when dealing with shifts in saturation and luminance (Yang et al., 2024). These drawbacks result from the fact that, unlike hue, saturation and luminance groups do not exhibit cyclic behavior.

In this paper, we propose hypertoroidal color equivariant network ($\mathbb{T}^3\text{CEN}$) that is perfectly equivariant to shifts in hue, saturation, and luminance by leveraging the geometric structure of the Hue-Saturation-Luminance (HSL) color space. We leverage topological covering to reformulate the saturation and luminance group such that they

Preprint. * Equal contribution. † Corresponding author. ² Work done as a visiting student at Princeton.

exhibit cyclic behavior that enables perfect equivariance. The improved structure of the network yields a more interpretable latent space which results in improved performance in image classification and segmentation tasks. We showcase the improved performance on both synthetic datasets with variation in one channel as well as large scale real world medical datasets, where T^3 CEN outperforms baseline equivariant and conventional architectures. Finally, we also show that the proposed double-cover can be applied to achieve perfect equivariance to geometric transformations such as scale.

2 Related Works

Group convolutional neural networks. The widespread adoption of convolutional networks for image processing task can partially be attributed to the improved generalization from planar translational equivariance. Many existing architectures have focuses on expanding the equivariance capacity of CNNs to additional symmetry groups (Kondor & Trivedi, 2018; Cohen et al., 2019b) such as rotation and scale. In their seminal work, Cohen & Welling (2016) introduced an architecture for finite group convolutions for 2D rotations and reflections by convolving inputs with the group orbit of the learned filter bank. Worrall et al. (2017) further introduced equivariance to continuous rotations by leveraging circular harmonic structure.

Group convolutional networks have also been designed to accommodate non-cyclic group such as scale symmetry (Esteves et al., 2017; Worrall & Welling, 2019; Sun & Blu, 2023) and groups acting on higher dimensions such as 3D rotations (Thomas et al., 2018; Esteves et al., 2019), Euclidean transformations (Batzner et al., 2022), and general manifolds (Cohen et al., 2019a). Leveraging symmetries that occur naturally in computer vision tasks, these group convolutional networks offer improved interpretability, generalizability, and data efficiency over conventional convolutional networks.

Learning under color imbalance. Existing studies have demonstrated the negative impact of color variance on classification tasks (Buhmester et al., 2019; De & Pedersen, 2021). Previous works attempt to address this challenge through data augmentation algorithms, such as AugMix (Hendrycks et al., 2019) and Deep Augment (Hendrycks et al., 2021), to artificially expand the training data. More structured and data efficient approaches leverage invariant architectures to improve robustness and generalization to changes in color and other perceptual quantities (Geusebroek et al., 2001; Chong et al., 2008; Lengyel et al., 2021; Pakzad et al., 2022; Hong et al., 2024). However, retaining color information can add an important cue in representation learning (Engilberge et al., 2017), which is in conflict with the main aim of color invariance.

Equivariant architectures resolve this conflict by retaining color information throughout the network. Lengyel et al. (2023) leverages this concept to propose convolutional layers that are equivariant to hue-shifts by rotating the RGB values of input images in the lifting layer. However, performing lifting directly on the input color space yields representations that are only approximately equivariant to only hue-shifts. Yang et al. (2024) resolves this drawback by performing lifting operations on the HSL color space to design a convolution layer that is equivariant to hue-, saturation-, and luminance-shifts. Hue is modeled with a cyclic group and saturation/luminance with a translation group, with learned representations that are exactly equivariant to hue-shift and only approximately so to saturation- and luminance-shifts.

Our proposed hypertoroidal color equivariant network differs from Yang et al. (2024) in two main aspects. First, we propose a new topological covering map that gives saturation and luminance groups cyclic characteristics; and second we use this covering to design a convolution network that is fully equivariant to shifts in hue, saturation, and luminance.

Topological covering. A covering is a map between topological spaces that intuitively projects multiple copies onto itself. A notable application of cover map is the double-cover from unit quaternions (\mathbb{S}^3) to 3D rotations ($SO(3)$) (Gallier & Quaintance, 2019). Covering maps can be leveraged to project a complex space to one with more desirable characteristics. Specifically, machine learning applications have leveraged covering maps to design well behaved convolutions on geometric surfaces (Maron et al., 2017; Haim et al., 2019) and characterize graph neural

network expressivity (Gallier & Quaintance, 2019; Garg et al., 2020). In this paper, we propose a convolutional network that is perfectly equivariant to color by leveraging a covering that enables perfect group convolutions for non-cyclic channels.

3 Background

This section reviews key concepts including groups, group actions, equivariance, group convolution, and the notion of a topological covering.

Groups and group actions. Group convolutional neural networks (GCNNs) Cohen & Welling (2016) demonstrate how the conventional planar CNN can be generalized to finite groups. Here, a *group* is defined as a set G together with a binary operation $\cdot : G \times G \rightarrow G$ that satisfies the following axioms:

1. *Associativity.* For $a, b, c \in G$, $(a \cdot b) \cdot c = a \cdot (b \cdot c)$,
2. *Existence of identity.* There exists an element $e \in G$, so that for any element $a \in G$, $e \cdot a = a \cdot e = a$,
3. *Existence of inverse.* For any element $a \in G$ there exists an element $b \in G$ so that $a \cdot b = b \cdot a = e$.

The elements of a group transform elements of a (left) G -set X , by the *group action* $\varphi : G \times X \rightarrow X$ which satisfies the following:

1. For all $a, b \in G$ and all $x \in X$, $\varphi(a, \varphi(b, x)) = \varphi(ab, x)$
2. For all $x \in X$, $\varphi(e, x) = x$.

Equivariance. An important characteristic of conventional planar CNNs is that they are equivariant to translation. Here, *equivariance* is defined as a relationship between two G -sets X and Y . Given the group actions $\varphi : G \times X \rightarrow X$ and $\phi : G \times Y \rightarrow Y$, a function $f : X \rightarrow Y$ is said to be equivariant, if and only if for all $x \in X$, and $a \in G$, $f(\varphi(a, x)) = \phi(a, f(x))$. Invariance is a special case of equivariance where $\phi(a, f(x)) = f(x)$.

Group convolution. In a conventional CNN, the feature map at layer l , denoted $f^l : \mathbb{Z}^2 \rightarrow \mathbb{R}^{K^l}$, is convolved with a set of K^{l+1} filters, denoted $\psi_i^l : \mathbb{Z}^2 \rightarrow \mathbb{R}^{K^l}$, where i ranges from 1 to K^{l+1} . The feature map f^{l+1} is the result of convolving feature map f^l with filters ψ_i^l ,

$$[f^l * \psi_i^l](x) = \sum_{y \in \mathbb{Z}^2} \sum_{k=1}^{K^l} f_k^l(y) \psi_{i,k}^l(x - y), \quad x \in \mathbb{Z}^2. \quad (1)$$

This operation can be shown to be equivariant to 2D translations. The more general group convolution,

$$[f^l * \psi_i^l](a) = \sum_{b \in G} \sum_{k=1}^{K^l} f_k^l(b) \psi_{i,k}^l(b^{-1}a), \quad a \in G, \quad (2)$$

can be shown to be equivariant to the action of the group G .

Topological covering. GCNNs are a powerful tool, but they require that symmetry transformation is a finite group. There are several contexts in which this requirement does not hold (e.g., color symmetry and scale symmetry). In cases where the symmetry is interval valued, we can construct a covering that can be used to lift the interval which is not a group to the circle which is a group. A map is a *covering map* iff it is smooth and surjective, and satisfies criteria for evenness (see Gallier & Quaintance (2020) for a precise definition).

4 Method

In this section we introduce our hypertoroidal color equivariant network ($\mathbb{T}^3\text{CEN}$). We present the definitions for the hue, saturation and luminance groups, and their group actions. Next we review HSL group convolution, and finally, we introduce our lifting layer and prove it is equivariant.

Hue group and group action. Following Yang et al. (2024), we identify elements of the discretized hue group H_N with elements of the cyclic group C_N . Given an HSL image $x = (x_h, x_s, x_l)$ where x_h , x_s , and x_l are the hue, saturation and luminance channels, we define the action of $h_i \in H_N$ on x as,

$$\varphi_h(h_i, x) = ((x_h + h_i) \pmod{255}, x_s, x_l), \quad (3)$$

where $(\cdot) \pmod{(\cdot)}$ denotes pixel-wise modulo. Given a function $f = (f_1, \dots, f_N)$ on H_N (e.g., a feature map, or a filter), we define the action of h_i on f as,

$$\phi_h(h_i, f) = (f_{(1+i) \pmod{N}}, \dots, f_{(N+i) \pmod{N}}). \quad (4)$$

Saturation group and group action. In the HSL color space, saturation values are restricted to an interval. Because the interval does not have group structure, it is not possible to construct an GCNN on this representation directly. To get around this, (Yang et al., 2024) model saturation with the structure of the translation group $(\mathbb{R}, +)$. An element s_i of resulting saturation group S_M , acts on HSL images by the group action

$$\varphi_s(s_i, x) = (x_h, \min(x_s + s_i, c), x_l), \quad (5)$$

and on S_M functions $f = (f_1, \dots, f_M)$ by the group action

$$\phi_s(s_i, f) = (f_{1+i}, \dots, f_M, \underbrace{\mathbf{0}, \dots, \mathbf{0}}_i). \quad (6)$$

However, because saturation values are bounded, enforcing the translation group requires value clipping (see equation (5) and (6)). Consequently, saturation transformations can introduce spurious artifacts making learned representations only approximately equivariant.

To remedy this, we model saturation with the structure of the cyclic group C_M . Given the interval of valid saturation values $I = [0, c]$, we first center the interval giving a new interval $\tilde{I} = I - c/2$, then we construct the saturation manifold \tilde{S} using the inverse of the double-cover $\pi : \mathbb{T}^1 \rightarrow \tilde{I}$, where $\pi(\theta) = \frac{c}{2} \sin \theta$. From there, we define the saturation group (S_M, \cdot) , where the set S_M of order M is determined by a uniform discretization of \tilde{S} , and the binary operation $\cdot : S_M \times S_M \rightarrow S_M$ is defined,

$$a \cdot b \mapsto (a + b) \pmod{2\pi}, \quad a, b \in S_M. \quad (7)$$

We also define the S_M group action on HSL images and functions on S_M . Given an HSL image $x = (x_h, x_s, x_l)$, we define the action of $s_i \in S_M$ on x by,

$$\varphi_s(s_i, x) = (x_h, \pi((x_s + s_i) \pmod{2\pi}), x_l), \quad (8)$$

and given a function $f = (f_1, \dots, f_M)$ on the discrete saturation group S_M , we define the action of s_i on f by,

$$\phi_s(s_i, f) = (f_{(1+i) \pmod{M}}, \dots, f_{(M+i) \pmod{M}}). \quad (9)$$

Luminance group and group action. In HSL, luminance values are also restricted to the interval. To give the luminance space group structure, we use the same strategy we used for the saturation space in the previous section. We denote the discretized luminance group L_R , the luminance group action on images $\varphi_l(l_i, x)$ and the luminance group action on an L_R function, $\phi_l(l_i, f)$ (see Appendix A.1 for additional details).

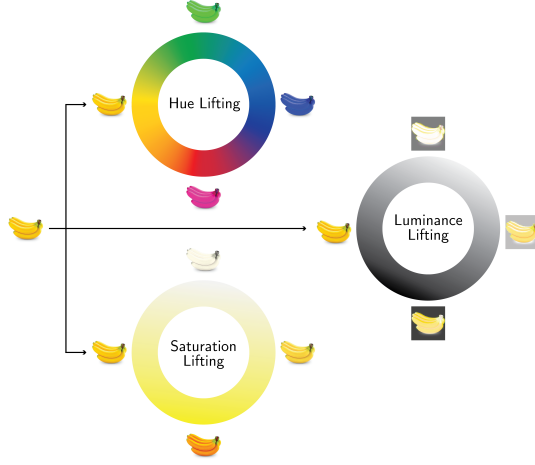


Figure 1: **Hue, saturation, and luminance lifting.** We lift an image with white background with respect to the hue, saturation, and luminance channels. **(Top)** Hue lifting of $\mathbb{T}^3\text{CEN}$, which follows the hue lifting proposed in Yang et al. (2024). **(Middle)** Luminance lifting of $\mathbb{T}^3\text{CEN}$ using a double-cover to give cyclic behavior to the luminance group. As the background is white, the double-cover will yields black/gray backgrounds. **(Bottom)** Saturation lifting of $\mathbb{T}^3\text{CEN}$ using a double-cover to give cyclic behavior to the saturation group.

HSL group and group Action. Having defined the hue, saturation and luminance groups, and their group actions, we can now define the HSL group and its group action. We define the HSL group as the product group $HSL_{NMR} := H_N \times S_M \times L_R$, and the HSL group actions as compositions of the hue, saturation, and luminance group actions. Concretely, given an HSL image x , we define the action of $g_{ijk} \in HSL_{NMR}$ on x by

$$\varphi_{hsl}(g_{ijk}, x) = \varphi_h(h_i, \varphi_s(s_j, \varphi_l(l_k, x))), \quad (10)$$

and given an HSL_{NMR} function $f = (f_{111}, \dots, f_{NMR})$, we define the action of g_{ijk} on f by

$$\phi_{hsl}(g_{ijk}, f) = \tilde{\varphi}_h\left(h_i, \tilde{\varphi}_s\left(s_j, \tilde{\varphi}_l(l_k, f)\right)\right), \quad (11)$$

where the modified hue, saturation, and luminance group actions are defined as,

$$\tilde{\varphi}_h(h_i, f) = (f_{(1+i)(\text{mod } N)::}, \dots, f_{(N+i)(\text{mod } N)::}), \quad (12)$$

$$\tilde{\varphi}_s(s_j, f) = (f_{:(1+j)(\text{mod } M)::}, \dots, f_{:(M+j)(\text{mod } M)::}), \quad (13)$$

$$\tilde{\varphi}_l(l_k, f) = (f_{::(1+k)(\text{mod } R)}, \dots, f_{::(R+k)(\text{mod } R)}). \quad (14)$$

Lifting layer. Group convolutional processing is defined between functions on the relevant group. To map input images x , to the HSL group we use an HSL lifting layer

$$f^0(g_{ijk}) = \varphi_{hsl}(g_{ijk}, x), \quad g_{ijk} \in HSL_{NMR} \quad (15)$$

The resulting feature map f^0 is a function on the HSL group and can be used in convolutional processing. Our lifting layer is distinguished from others in the literature in that it can be applied to spaces that have interval structure. Since inputs to the group convolution operator must have group structure, our lifting layer first constructs a double-cover of the interval, to give a resulting space that is isomorphic to \mathbb{T}^1 (see paragraph Saturation group and group action for additional details). The interval is not a group but \mathbb{T}^1 is, and from here we can use a conventional lifting approach to realize a function on the HSL group. Our proposed HSL lifting layer is illustrated in Figure 1.

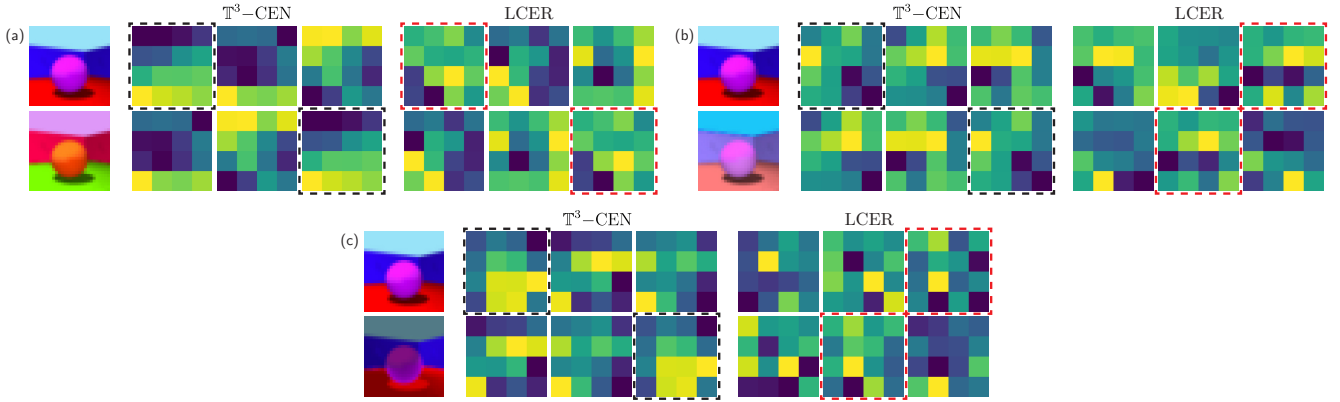


Figure 2: $\mathbb{T}^3\text{CEN}$ and **LCER** feature maps under **HSL** shifts. The features maps of $\mathbb{T}^3\text{CEN}$ are equivariant to shifts in hue, saturation, and luminance, while the feature maps of **LCER** are only equivariant to shifts in hue. **(a)** The images are related by a 90° hue rotation. **(b)** The images are related by a 0.5 shift in saturation. **(c)** The images are related by a 0.5 shift in luminance. In all cases, because our $\mathbb{T}^3\text{CEN}$ network is equivariant to color shifts (i.e., hue, saturation, and luminance shifts), the feature maps transform predictably (cyclically permuted). Conversely, **LCER** is only equivariant to hue shifts.

HSL group convolution. Lifted inputs are function on the HSL group and can convolved with other functions on the HSL group (e.g., HSL filters). Using the definition of group convolution in Equation (2), we define the HSL group convolution as

$$[f^l * \psi_i^l](a) = \sum_{r \in \text{HSL}} \sum_{k=1}^{K^l} f_k^l(r) \psi_{i,k}^l(r^{-1}a). \quad (16)$$

It can be shown that the HSL group convolution is equivariant to hue, saturation and luminance.

5 Experiments

In this section, we compare our $\mathbb{T}^3\text{CEN}$ to various color equivariant and non-equivariant baselines. We show that our model has lower equivariance error than other models on synthetic datasets, and better robustness to color shift on real datasets. We also analyze our double-cover lifting layer, quantifying coverage of the transformation space, and introducing a principled approach for selecting group order based on dataset characteristic. Finally, we demonstrate the utility of our double-cover lifting layer in the contexts of RGB color, and scaling transformations.

5.1 Equivariance Error

We first compare the equivariance error of our approach and the state-of-the-art color equivariant method, which we denote as **LCER** Yang et al. (2024). We do this both qualitatively and quantitatively. In our qualitative assessment, we take synthetically generated images from the 3D Shapes dataset (Kim & Mnih, 2018) and transform them in hue, saturation and luminance. If the proposed group actions are color equivariant, we should observe a commutative relationship between transformations of the input and transformations of their respective feature maps. We show the results of this experiment in Figures 2(a) 2(b) and 2(c). Our method preserves equivariance for all subgroups of the HSL group, while **LCER** only preserves equivariance for hue shifts.

In our quantitative assessment, we compute the saturation equivariance error. Following from Yang et al. (2024), we define the saturation equivariance error

$$\Delta_{\varphi_s} = \frac{|f(\varphi_s(s_i, x)) - \phi_s(s_i, f(x))|}{|f(\varphi_s(s_i, x)) + \phi_s(s_i, f(x))|}. \quad (17)$$



Figure 3: **Saturation equivariance error.** The normalized saturation equivariance error for $\mathbb{T}^3\text{CEN}$ and LCER is reported. $\mathbb{T}^3\text{CEN}$ has average error of 4.66×10^{-6} while LCER has average error of 0.445.

We plot the saturation equivariance error as a function of the saturation group order $M \in \{3, 5, 7, 9, 11, 15\}$ in Figure 3. The average error of our model is 4.66×10^{-6} and the average error of LCER is 0.445. We attribute this difference in equivariance error to the lifting error of LCER. We quantitatively measure the lifting error of the proposed group actions using the mean of the difference $\|x - \phi(g^{-1}, \phi(g, x))\|$. The lifting error of our model and LCER are compared Figure 4, where our lifting error is six orders of magnitude lower than LCER.

5.2 Generalization to Color shift

Embedding color equivariance allows for out-of-distribution (OOD) generalization. By using group actions that are compatible with the transformation space we achieve better generalization performance than existing methods.

Hue shift. We first evaluate our performance using the OOD hue shift experiments introduced in LCER Yang et al. (2024). We use the 3D Shapes dataset which contains synthetically generated RGB images of 3D shapes, where the color of the shape, floor, and walls vary across examples, as does the scale and orientation of the shape (see Appendix D.1 for details). The performance of $\mathbb{T}^3\text{CEN}$, CEConv (Lengyel et al., 2023), LCER (Yang et al., 2024), and ResNet44 (He et al., 2016) are reported in Table 1. In all cases, the classification accuracy of $\mathbb{T}^3\text{CEN}$ is on par or better than existing methods.

Saturation shift. We similarly evaluate the generalization performance of $\mathbb{T}^3\text{CEN}$, CEConv, LCER, and ResNet44 to saturation shifts. For this experiment we introduce a saturation shifted variation of the 3D Shapes dataset (see Appendix D.2 for details). The classification performance of all networks is reported in Table 2. We find that $\mathbb{T}^3\text{CEN}$ has significantly better classification accuracy than all baselines.

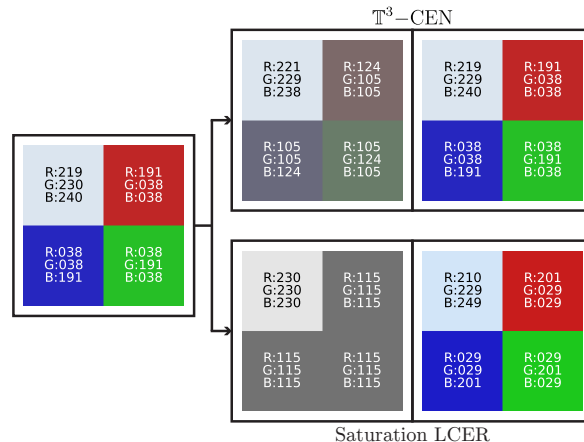


Figure 4: **Lifting error comparison.** An input images is lifted to the respective saturation group, shifted down by 0.75, and shifted up by 0.75. We compare the restored and original input image for $\mathbb{T}^3\text{CEN}$ (**top**) and LCER (**bottom**). The average 8-bit integer RGB error is 6.33×10^{-6} for $\mathbb{T}^3\text{CEN}$ and 8.65 for LCER.

Table 1: **Generalization to hue shift.** Classification error on the 3D Shapes datasets is reported. The models are evaluated on in-distribution (A/A), global out-of-distribution (A/B) and local out-of-distribution (A/C) test sets. $\mathbb{T}^3\text{CEN}$ performs on par with LCER and achieves improved generalization performance over ResNet and CEConv.

	ResNet44	CEConv-3	CEConv-4	LCER-H3	LCER-H4	$\mathbb{T}^3\text{CEN-H3}$	$\mathbb{T}^3\text{CEN-H4}$
A/A	0.00	0.00	0.00	0.00	0.00	0.00	0.00
A/B	51.25	0.02	0.60	0.03	0.00	0.03	0.00
A/C	26.66	0.05	0.53	0.04	0.00	0.04	0.00
Param	2.6M	3.8M	4.9M	2.6M	2.6M	2.6M	2.6M

Table 2: **Generalization to saturation shift.** Classification error on the saturation shifted 3D Shapes datasets is reported. The models are evaluated on in-distribution (A/A), random saturation shifts (A/B), and component-wise saturation shifts (A/C) test sets. $\mathbb{T}^3\text{CEN}$ achieve improved generalization performance over LCER and ResNet.

	ResNet44	LCER-S3	$\mathbb{T}^3\text{CEN-S3}$
A/A	0.00	0.00	0.00
A/B	41.40	0.00	0.00
A/C	42.20	0.04	0.00
Param	2.6M	2.6M	2.6M

Table 3: **Generalization to luminance shift.** Classification error on the small NORB dataset is reported. The models are evaluated on medium lighting (A/A), low lighting (A/B), and bright lighting (A/C) test sets. $\mathbb{T}^3\text{CEN}$ achieves improved generalization performance over LCER and ResNet. Moreover, with the same order, $\mathbb{T}^3\text{CEN-L3}$ outperforms LCER-L3.

	ResNet-18	LCER-L3	$\mathbb{T}^3\text{CEN-L3}$	$\mathbb{T}^3\text{CEN-L4}$	$\mathbb{T}^3\text{CEN-L8}$	$\mathbb{T}^3\text{CEN-L16}$
A/A	8.32	7.31	5.36	6.60	5.67	<u>5.66</u>
A/B	37.70	34.83	14.42	13.09	<u>11.88</u>	11.09
A/C	33.88	36.43	31.53	29.53	<u>27.46</u>	24.32
Param	11.2M	11.1M	11.2M	11.2M	11.1M	11.2M

Luminance shift. We evaluate the generalization performance of $\mathbb{T}^3\text{CEN}$, LCER, and ResNet18 to luminance shifts on the small NORB dataset (LeCun et al., 2004) (see Appendix D.4 for details). The classification performance of all networks is reported in Table 3. We find that $\mathbb{T}^3\text{CEN}$ has significantly better classification accuracy than all baselines.

HSL shift. We evaluate the generalization performance of $\mathbb{T}^3\text{CEN}$, LCER, and ResNet18 to HSL shifts on our HSL shifted 3D Shapes dataset (see Appendix D.3 for details). The classification performance of all networks is reported in Table 4. In contrast to baseline models, HSL-equivariant $\mathbb{T}^3\text{CEN-H4S4L4}$ achieves perfect classification accuracy.

Color shift in the wild. We evaluate the classification performance of $\mathbb{T}^3\text{CEN}$ on the Caltech-101 (Li et al., 2022), Oxford-IIT Pets (Parkhi et al., 2012), Stanford Cars (Krause et al., 2013), STL-10 (Coates et al., 2011), CIFAR-10 and CIFAR-100 (Krizhevsky & Hinton, 2009) datasets (see Appendix D). We assess generalization performance on saturation and luminance shifted versions of these datasets. Results are shown in Table 5. The generalization performance of $\mathbb{T}^3\text{CEN}$ consistently exceeds that of baseline models.

5.3 Robustness to Color Imbalance.

We evaluate the robustness of $\mathbb{T}^3\text{CEN}$ to color imbalance on the Camelyon17 histopathology classification dataset (Bandi et al., 2018). The Camelyon17 dataset contains images of human tissue gathered from five distinct hospitals where variations arise from differences in data collection methodologies and processing procedures. Additional dataset details are provided in Appendix D.

Table 4: **Generalization to HSL shift.** Classification error on the HSL shifted 3D Shapes dataset is reported. \mathbb{T}^3 CEN achieves improved generalization performance of LCER and ResNet.

	ResNet44	LCER-H4S3	\mathbb{T}^3 CEN-H3S3L3	\mathbb{T}^3 CEN-H4S4L4
Error	55.40 (2.19)	9.76 (3.54)	3.01 (1.61)	0.00 (0.00)
Param	2.6M	2.6M	2.6M	2.6M

Table 5: **Generalization to color shift.** Classification error on the Caltech-101, CIFAR-10, CIFAR-100, Oxford-IIT Pets, Stanford Cars, STL-10 datasets are reported. \mathbb{T}^3 CEN achieves improved generalization performance over baselines on saturation and luminance shifted testsets, where saturation and luminance were reduced by 0.5. Performance on the vanilla datasets are reported in Table 7 where \mathbb{T}^3 CEN performs on par with LCER and outperforms baselines. See Appendix D for details on dataset and training.

Network	Caltech 101	CIFAR-10	CIFAR-100	Stanford Cars	Oxford Pets	STL-10
Saturation Shifted Dataset						
ResNet	56.29 (0.59)	<u>11.71 (1.16)</u>	47.58 (5.19)	37.34 (3.75)	57.92 (2.49)	30.28 (0.76)
ResNet-aug	49.04 (0.63)	11.91 (0.58)	43.13 (2.13)	32.00 (6.41)	51.88 (1.05)	28.86 (0.40)
LCER-H4	48.85 (1.72)	14.28 (2.24)	48.57 (0.35)	<u>31.16 (2.72)</u>	50.65 (4.65)	25.05 (2.16)
LCER-S3	43.16 (1.57)	13.28 (1.29)	45.90 (1.08)	40.78 (3.01)	<u>46.92 (0.95)</u>	27.53 (1.52)
\mathbb{T}^3 CEN-H4	48.85 (1.72)	14.28 (2.24)	48.57 (0.35)	<u>31.16 (2.72)</u>	50.65 (4.65)	25.05 (2.16)
\mathbb{T}^3 CEN-S4	<u>42.24 (1.45)</u>	11.59 (1.33)	<u>44.27 (1.70)</u>	42.91 (5.11)	48.70 (1.46)	21.00 (1.45)
\mathbb{T}^3 CEN-L4	54.00 (1.45)	14.35 (0.57)	49.13 (2.52)	34.25 (8.41)	59.55 (3.20)	33.26 (3.44)
\mathbb{T}^3 CEN-H4S4	40.02 (2.91)	13.64 (0.52)	46.23 (0.85)	40.36 (8.34)	38.91 (2.86)	22.31 (1.91)
\mathbb{T}^3 CEN-S4L4	46.04 (5.71)	14.13 (0.57)	45.99 (1.70)	29.83 (1.33)	54.03 (6.96)	<u>24.63 (5.65)</u>
Luminance Shifted Dataset						
ResNet	73.91 (1.66)	36.79 (3.40)	69.39 (6.24)	83.68 (2.96)	80.61 (0.34)	56.92 (1.94)
ResNet-aug	30.82 (1.20)	63.63 (2.33)	59.17 (1.28)	71.38 (5.46)	74.05 (2.49)	51.83 (1.19)
LCER-H4	72.17 (2.78)	39.81 (6.03)	74.83 (0.87)	76.19 (0.83)	75.38 (1.96)	53.45 (0.76)
LCER-L3	<u>49.55 (2.07)</u>	<u>25.62 (3.78)</u>	51.34 (2.16)	66.51 (4.57)	<u>64.04 (1.72)</u>	<u>40.13 (1.18)</u>
\mathbb{T}^3 CEN-H4	72.17 (2.78)	39.81 (6.03)	74.83 (0.87)	76.19 (0.83)	75.38 (1.96)	53.45 (0.76)
\mathbb{T}^3 CEN-S4	70.36 (0.49)	40.31 (6.03)	71.39 (1.71)	62.70 (5.17)	79.47 (2.21)	55.25 (2.34)
\mathbb{T}^3 CEN-L4	50.41 (1.59)	25.33 (1.54)	<u>52.57 (1.16)</u>	81.42 (6.55)	66.40 (2.82)	38.01 (2.21)
\mathbb{T}^3 CEN-H4L4	46.23 (1.25)	39.25 (4.55)	58.35 (1.14)	55.55 (6.83)	67.97 (4.58)	55.48 (1.07)
\mathbb{T}^3 CEN-S4L4	50.28 (3.31)	27.21 (0.97)	56.71 (3.04)	<u>61.21 (4.18)</u>	62.85 (2.63)	41.63 (1.53)

We compare our classification performance to ResNet50 (He et al., 2016), CEConv, and LCER in Table 6. The saturation equivariant versions of \mathbb{T}^3 CEN and LCER show the best performance. We attribute this to color imbalance in the dataset. Specifically, dataset statistics show that saturation varies non-uniformly across the dataset (see Appendix D.6).

In all experiments, we maintain a fixed number of network parameters across all HSL configurations. To do this, we reduce filter depth when increasing HSL order. In some cases this can lead to reduced network capacity. Consequently, networks with higher order may perform worse than networks with lower order (e.g., compare the classification accuracy of \mathbb{T}^3 CEN-S4 and \mathbb{T}^3 CEN-H4S4 in Table 6).

To quantify this effect, we evaluate the OOD classification performance of hue equivariant networks of different orders on the hue-shift MNIST (LeCun et al., 2002) dataset. Figure 8 in Appendix C.1 shows how classification accuracy varies with order. With increasing hue order, accuracy increases from 86.06% to 98.04%, then decreases. Interestingly, the highest classification accuracy occurs when the hue group order has the highest entropy per element (see Section 5.4 and Figure 6 for details).

Table 6: **Generalization to color shift in Camelyon17.** Classification error on the Camelyon17 dataset is reported. $\mathbb{T}^3\text{CEN}$ achieves improved generalization performance over LCER and ResNet.

	ResNet50	CEConv-3	LCER-H4	LCER-S3	LCER-H4S3	$\mathbb{T}^3\text{CEN-H4}$
Error	28.91 (7.58)	28.76 (9.93)	27.53 (3.39)	<u>16.08 (2.68)</u>	19.06 (4.92)	27.53 (3.39)
Param	23.5M	23.1M	23.5M	23.3M	23.0M	23.5M
	$\mathbb{T}^3\text{CEN-S4}$	$\mathbb{T}^3\text{CEN-L4}$	$\mathbb{T}^3\text{CEN-H4S4}$	$\mathbb{T}^3\text{CEN-S4L4}$	$\mathbb{T}^3\text{CEN-H4S4L4}$	
Error	12.11 (2.19)	21.88 (2.28)	20.95 (6.75)	16.70 (5.44)	19.97 (1.25)	
Param	23.5M	23.5M	23.5M	23.5M	23.5M	

5.4 Double-Cover Lifting Layer

Analyzing lifting layer coverage. A key contribution of our method is our double-cover lifting layer. By lifting interval valued symmetries (e.g., saturation, luminance) to the circle, we can impart group structure and design group convolutional architectures that are perfectly equivariance. However, while our lifting layer covers \mathbb{T}^1 uniformly, how well it covers the interval is input dependent. We measure interval coverage by the entropy of the partitioning. For the interval $(0, c)$ with the partitioning $(0, p_1, p_2, \dots, p_{N-1}, p_N, c)$, the entropy of this partition is defined to be

$$H = \frac{1}{c} \sum_{i=1}^{N-1} v_i \log v_i, \quad v_i = p_{i+1} - p_i. \quad (18)$$

We analyze interval coverage for the case of $N = 4$ in Figure 5. Maximum coverage occurs when the input value is $kc/N - c/2N$, where $k \in \mathbb{N}$ and $k \leq N$.

Degenerate lifting. Degenerate cases occur when the input value is kc/N , where $k \in \mathbb{N}$ and $k \leq N$. In degenerate cases, our lifting layer yields repeated values

$$\left[0, \frac{c}{N}, 2\frac{c}{N}, \dots, c, \dots, 2\frac{c}{N}, \frac{c}{N}\right]. \quad (19)$$

In this case, the lifting will yield at most $N/2 + 1$ representations with useful information.

Selecting the right order. We define the best order for a particular interval to be the order with the highest average coverage H/N . This metric offers a principled way to select the network order using input data statistics. Figure 6 shows the average coverage across a range of orders. For most cases, the highest average coverage is achieved at order four.

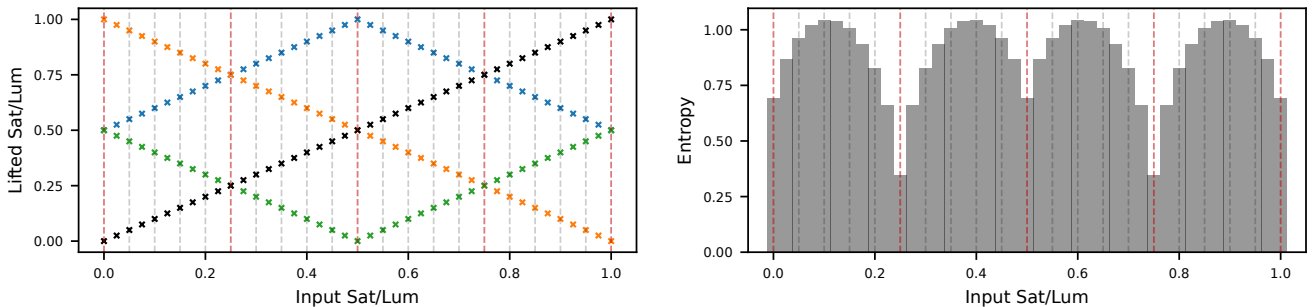


Figure 5: **Lifting coverage and cases of degenerate lifting.** (Top) Coverage of the lifted representation for different input saturation/luminance. The original input value is denoted with black and the first, second, and third lifted representation is in blue, orange, and green. (Bottom) Information entropy of the lifted representation. Cases of degenerate lifting is highlighted vertically in red.

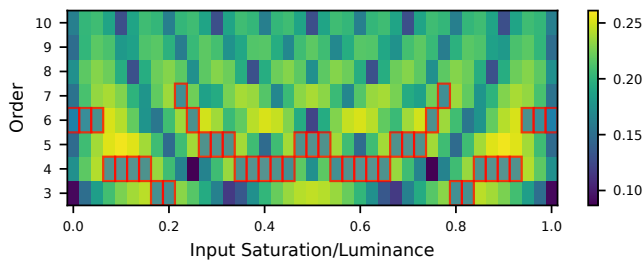


Figure 6: **Lifting entropy density.** We show the entropy density (information entropy divided by order) at different order and input saturation/luminance. The order with the highest entropy density for every input is highlighted with red boxes.

Application to RGB shift equivariance. Our double-cover lifting layer can also be used to design for equivariance to RGB shifts. Given the interval of valid RGB values $I = [0.0, 1.0]$, we use our lifting layer as described in Section 4 to define the RGB group and group actions. Given an RGB image $x = (x_r, x_g, x_b)$, we define the group action of $g_{ijk} \in RGB_{NMR}$ on x by,

$$\varphi_{rgb}(g_{ijk}, x) = \varphi_r(r_i, \varphi_g(g_j, \varphi_b(b_k, x))), \quad (20)$$

where the red, green, and blue group actions are defined as,

$$\varphi_r(r_i, x) = (\pi((x_r + r_i) \bmod 2\pi), x_g, x_b), \quad (21)$$

$$\varphi_g(g_i, x) = (x_r, \pi((x_g + g_i) \bmod 2\pi), x_b), \quad (22)$$

$$\varphi_b(b_i, x) = (x_r, x_g, \pi((x_b + b_i) \bmod 2\pi)). \quad (23)$$

To show the group actions are equivariant we qualitatively test for commutativity for both LCER and T^4CEN . Figure 7 shows that a the feature maps of a red shifted input image are equal to the shifted feature maps of the

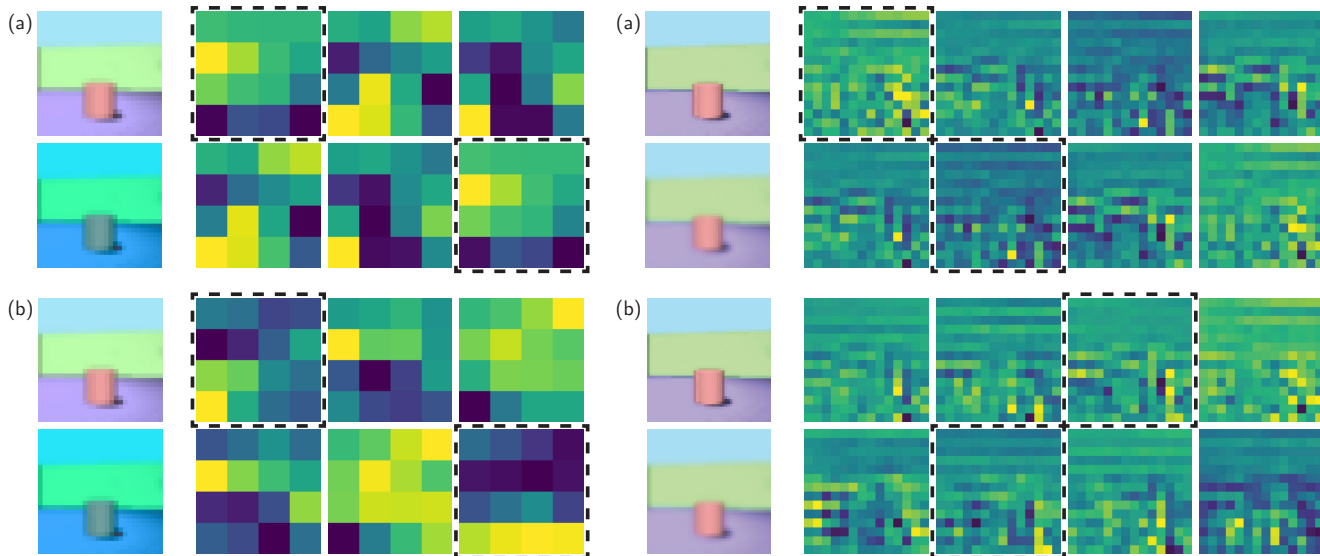


Figure 7: **T^3CEN equivariant feature map under RGB shift and under scale.** (Left) To show the group actions are equivariant we qualitatively test for commutativity for both LCER and T^4CEN . We demonstrate that the feature maps of (a) T^3CEN is equivariant to shifts to the RGB channels while that of (b) LCER is not. (Right) To show the group actions are equivariant we qualitatively test for commutativity for both LCER and T^4CEN . We demonstrate that the feature maps of (a) T^3CEN is equivariant to shifts in scaling while that of (b) LCER is not.

original input image, thus satisfying the commutativity relationship. While this application shows it is possible to use design a color equivariant network in the RGB color space, this option may have poorer performance than a HSL color equivariant network since degenerate lifts can be observed on all three channels.

Application to scale equivariance. The proposed covering map can similarly be used to design for equivariance to scale (resolution) transformations. Given the interval of valid intrinsic scale is $I = [0.0, 1.0]$ (Hosu et al., 2025), we use our lifting layer as described in Section 4 to define the scale (\mathcal{A}) group and group actions. Given an image with pixel location $x = (p_x, p_y)$, we define the group action of $\alpha_i \in \mathcal{A}_N$ on x by,

$$\varphi_\alpha(\alpha_i, x) = \left(\pi((p_x + g_i) \bmod 2\pi), \pi((p_y + \alpha_i) \bmod 2\pi) \right). \quad (24)$$

To show the group actions are equivariant we qualitatively test for commutativity for both LCER and \mathbb{T}^4 CEN. Figure 7 shows that the feature maps of a downsampled input image are equal to the shifted feature maps of the original input image, thus satisfying the commutativity relationship.

6 Conclusion

In this paper we introduce \mathbb{T}^3 CEN, a hypertoroidal color equivariant network. To ensure perfect color equivariance, we use a double-cover lifting layer which can give group structure to interval valued quantities (e.g., saturation, and luminance). We show that our lifting layer preserves equivariance better than existing methods, and eliminates approximation artifacts. This translates into higher prediction accuracy in the presence of color shift, and color imbalance. We also show the broad utility of our double-cover lifting layer. Beyond the interval valued symmetries of saturation and luminance, our lifting layer can also be used to build color equivariant architectures in the RGB space, and scale equivariant architectures.

Limitations. The primary limitation of approach is computation expense. GCNN are typically more computationally expensive than conventional networks due to the filter orbit needed to approximate a continuous group (Cohen & Welling, 2016). The computational expense of GCNNs is roughly equal to conventional networks with a filter bank size that matches the augmented filter orbit of the GCNN.

References

- Peter Bandi, Oscar Geessink, Quirine Manson, Marcory Van Dijk, Maschenka Balkenhol, Meyke Hermsen, Babak Ehteshami Bejnordi, Byungjae Lee, Kyunghyun Paeng, Aoxiao Zhong, et al. From detection of individual metastases to classification of lymph node status at the patient level: the camelyon17 challenge. *IEEE transactions on medical imaging*, 38(2):550–560, 2018.
- Simon Batzner, Albert Musaelian, Lixin Sun, Mario Geiger, Jonathan P Mailoa, Mordechai Kornbluth, Nicola Molinari, Tess E Smidt, and Boris Kozinsky. E (3)-equivariant graph neural networks for data-efficient and accurate interatomic potentials. *Nature communications*, 13(1):2453, 2022.
- Inês Bramão, Alexandra Reis, Karl Magnus Petersson, and Luís Faísca. The role of color information on object recognition: A review and meta-analysis. *Acta psychologica*, 138(1):244–253, 2011.
- Vanessa Buhrmester, David Münch, Dimitri Bulatov, and Michael Arens. Evaluating the impact of color information in deep neural networks. In *Iberian conference on pattern recognition and image analysis*, pp. 302–316. Springer, 2019.
- Hamilton Y Chong, Steven J Gortler, and Todd Zickler. A perception-based color space for illumination-invariant image processing. *ACM Transactions on Graphics (TOG)*, 27(3):1–7, 2008.

- Adam Coates, Andrew Ng, and Honglak Lee. An analysis of single-layer networks in unsupervised feature learning. In *Proceedings of the Fourteenth International Conference on Artificial Intelligence and Statistics (AISTATS)*, volume 15 of *JMLR Workshop and Conference Proceedings*, pp. 215–223, 2011.
- Taco Cohen and Max Welling. Group equivariant convolutional networks. In *International conference on machine learning*, pp. 2990–2999. PMLR, 2016.
- Taco Cohen, Maurice Weiler, Berkay Kicanaoglu, and Max Welling. Gauge equivariant convolutional networks and the icosahedral cnn. In *International conference on Machine learning*, pp. 1321–1330. PMLR, 2019a.
- Taco S Cohen, Mario Geiger, and Maurice Weiler. A general theory of equivariant cnns on homogeneous spaces. *Advances in neural information processing systems*, 32, 2019b.
- Kanjar De and Marius Pedersen. Impact of colour on robustness of deep neural networks. In *Proceedings of the IEEE/CVF international conference on computer vision*, pp. 21–30, 2021.
- Martin Engilberge, Edo Collins, and Sabine Süsstrunk. Color representation in deep neural networks. In *2017 IEEE International Conference on Image Processing (ICIP)*, pp. 2786–2790. IEEE, 2017.
- Carlos Esteves, Christine Allen-Blanchette, Xiaowei Zhou, and Kostas Daniilidis. Polar transformer networks. *arXiv preprint arXiv:1709.01889*, 2017.
- Carlos Esteves, Yinshuang Xu, Christine Allen-Blanchette, and Kostas Daniilidis. Equivariant multi-view networks. In *Proceedings of the IEEE/CVF international conference on computer vision*, pp. 1568–1577, 2019.
- Jean Gallier and Jocelyn Quaintance. Linear algebra for computer vision, robotics, and machine learning. *University of Pennsylvania*, 2019.
- Jean Quaintance Gallier and Jocelyn Quaintance. *Differential Geometry and Lie Groups*, volume 12. Springer, 2020.
- Vikas Garg, Stefanie Jegelka, and Tommi Jaakkola. Generalization and representational limits of graph neural networks. In *International conference on machine learning*, pp. 3419–3430. PMLR, 2020.
- J-M Geusebroek, Rein Van den Boomgaard, Arnold W. M. Smeulders, and Hugo Geerts. Color invariance. *IEEE Transactions on Pattern analysis and machine intelligence*, 23(12):1338–1350, 2001.
- Ali Güneş, Habil Kalkan, and Efkan Durmuş. Optimizing the color-to-grayscale conversion for image classification. *Signal, Image and Video Processing*, 10(5):853–860, 2016.
- Niv Haim, Nimrod Segol, Heli Ben-Hamu, Haggai Maron, and Yaron Lipman. Surface networks via general covers. In *Proceedings of the IEEE/CVF international conference on computer vision*, pp. 632–641, 2019.
- Kaiming He, Xiangyu Zhang, Shaoqing Ren, and Jian Sun. Deep residual learning for image recognition. In *Proceedings of the IEEE conference on computer vision and pattern recognition*, pp. 770–778, 2016.
- Dan Hendrycks, Norman Mu, Ekin D Cubuk, Barret Zoph, Justin Gilmer, and Balaji Lakshminarayanan. Augmix: A simple data processing method to improve robustness and uncertainty. *arXiv preprint arXiv:1912.02781*, 2019.
- Dan Hendrycks, Steven Basart, Norman Mu, Saurav Kadavath, Frank Wang, Evan Dorundo, Rahul Desai, Tyler Zhu, Samyak Parajuli, Mike Guo, et al. The many faces of robustness: A critical analysis of out-of-distribution generalization. In *Proceedings of the IEEE/CVF international conference on computer vision*, pp. 8340–8349, 2021.
- Mingbo Hong, Shen Cheng, Haibin Huang, Haoqiang Fan, and Shuaicheng Liu. You only look around: Learning illumination-invariant feature for low-light object detection. *Advances in Neural Information Processing Systems*, 37:87136–87158, 2024.

- Vlad Hosu, Lorenzo Agnolucci, Daisuke Iso, and Dietmar Saupe. Image intrinsic scale assessment: Bridging the gap between quality and resolution. *arXiv preprint arXiv:2502.06476*, 2025.
- Hyunjik Kim and Andriy Mnih. Disentangling by factorising. In *International conference on machine learning*, pp. 2649–2658. PMLR, 2018.
- Diederik P Kingma. Adam: A method for stochastic optimization. *arXiv preprint arXiv:1412.6980*, 2014.
- Risi Kondor and Shubhendu Trivedi. On the generalization of equivariance and convolution in neural networks to the action of compact groups. In *International conference on machine learning*, pp. 2747–2755. PMLR, 2018.
- Jonathan Krause, Michael Stark, Jia Deng, and Li Fei-Fei. 3d object representations for fine-grained categorization. In *Proceedings of the IEEE International Conference on Computer Vision Workshops (ICCVW)*, pp. 554–561, 2013. doi: 10.1109/ICCVW.2013.77.
- Alex Krizhevsky and Geoffrey Hinton. Learning multiple layers of features from tiny images. Technical report, University of Toronto, 2009.
- Yann LeCun, Léon Bottou, Yoshua Bengio, and Patrick Haffner. Gradient-based learning applied to document recognition. *Proceedings of the IEEE*, 86(11):2278–2324, 2002.
- Yann LeCun, Fu Jie Huang, and Léon Bottou. Learning methods for generic object recognition with invariance to pose and lighting. *Proceedings of the 2004 IEEE Computer Society Conference on Computer Vision and Pattern Recognition*, 2:II–104 Vol.2, 2004.
- Attila Lengyel, Sourav Garg, Michael Milford, and Jan C van Gemert. Zero-shot day-night domain adaptation with a physics prior. In *Proceedings of the IEEE/CVF International Conference on Computer Vision*, pp. 4399–4409, 2021.
- Attila Lengyel, Ombretta Strafforello, Robert-Jan Bruintjes, Alexander Gielisse, and Jan van Gemert. Color equivariant convolutional networks. *Advances in Neural Information Processing Systems*, 36:29831–29850, 2023.
- Fei-Fei Li, Marco Andreoto, Marc’Aurelio Ranzato, and Pietro Perona. Caltech 101. <https://data.caltech.edu/records/20086>, April 2022. Dataset.
- Haggai Maron, Meirav Galun, Noam Aigerman, Miri Trope, Nadav Dym, Ersin Yumer, Vladimir G Kim, and Yaron Lipman. Convolutional neural networks on surfaces via seamless toric covers. *ACM Trans. Graph.*, 36(4):71–1, 2017.
- Arezou Pakzad, Kumar Abhishek, and Ghassan Hamarneh. Circle: Color invariant representation learning for unbiased classification of skin lesions. In *European Conference on Computer Vision*, pp. 203–219. Springer, 2022.
- Omkar M. Parkhi, Andrea Vedaldi, Andrew Zisserman, and C. V. Jawahar. The oxford-iiit pet dataset. <https://www.robots.ox.ac.uk/~vgg/data/pets/>, 2012. Dataset.
- Zikai Sun and Thierry Blu. Empowering networks with scale and rotation equivariance using a similarity convolution. *arXiv preprint arXiv:2303.00326*, 2023.
- Nathaniel Thomas, Tess Smidt, Steven Kearnes, Lusann Yang, Li Li, Kai Kohlhoff, and Patrick Riley. Tensor field networks: Rotation-and translation-equivariant neural networks for 3d point clouds. *arXiv preprint arXiv:1802.08219*, 2018.
- Daniel Worrall and Max Welling. Deep scale-spaces: Equivariance over scale. *Advances in Neural Information Processing Systems*, 32, 2019.
- Daniel E Worrall, Stephan J Garbin, Daniyar Turmukhambetov, and Gabriel J Brostow. Harmonic networks: Deep translation and rotation equivariance. In *Proceedings of the IEEE conference on computer vision and pattern recognition*, pp. 5028–5037, 2017.

Yiting Xie and David Richmond. Pre-training on grayscale imagenet improves medical image classification. In *Proceedings of the European conference on computer vision (ECCV) workshops*, pp. 0–0, 2018.

Yulong Yang, Felix O’Mahony, and Christine Allen-Blanchette. Learning color equivariant representations. *arXiv preprint arXiv:2406.09588*, 2024.

A Method

A.1 Luminance Group and Group Action

In the HSL color space, luminance values are restricted to an interval. Because the interval does not have group structure, it is not possible to construct an GCNN on this representation directly. To get around this, (Yang et al., 2024) model luminance with the structure of the translation group $(\mathbb{R}, +)$. An element l_i of resulting luminance group L_R , acts on HSL images by the group action

$$\varphi_l(l_i, x) = (x_h, x_s, \min(x_l + l_i, c)), \quad (25)$$

and on L_R functions $f = (f_1, \dots, f_R)$ by the group action

$$\phi_l(l_i, f) = (f_{1+i}, \dots, f_R, \underbrace{\mathbf{0}, \dots, \mathbf{0}}_i). \quad (26)$$

However, because luminance values are bounded, enforcing the translation group requires value clipping (see equation (25) and (26)). Consequently, luminance transformations can introduce spurious artifacts making learned representations only approximately equivariant.

To remedy this, we model luminance with the structure of the cyclic group C_R . Given the interval of valid luminance values $I = [0, c]$, we define the luminance manifold \tilde{L} using the inverse of the double-cover $\pi : \mathbb{T}^1 \rightarrow I$, where $\pi(\theta) = c \sin \frac{\theta}{2}$. From there, we are able to define the luminance group (L_R, \cdot) . The set L_R of cardinality R is determined by a uniform discretization of \tilde{L} , and the binary operation $\cdot : L_R \times L_R \rightarrow L_R$ is defined,

$$a \cdot b \mapsto (a + b) \bmod 2\pi, \quad a, b \in L_R. \quad (27)$$

We can also define the L_R group action on HSL images and functions on L_R . Given an HSL image $x = (x_h, x_s, x_l)$, we define the action of $l_i \in L_R$ on x by,

$$\varphi_l(l_i, x) = (x_h, x_s, \pi((x_l + l_i) \bmod 2\pi)), \quad (28)$$

and given a function $f = (f_1, \dots, f_R)$ on the discrete saturation group L_R , we define the action of an element l_i on f by,

$$\phi_l(l_i, f) = (f_{(1+i) \bmod R}, \dots, f_{(R+i) \bmod R}). \quad (29)$$

B Hue-Saturation-Luminance Group

In this section, we show that the hue, saturation, and luminance groups satisfies the axioms of a group. Recall that a *group* is defined as a set G together with a binary operation $\cdot : G \times G \rightarrow G$ that satisfies the following axioms:

1. *Associativity.* For $a, b, c \in G$, $(a \cdot b) \cdot c = a \cdot (b \cdot c)$,
2. *Existence of identity.* There exists an element $e \in G$, so that for any element $a \in G$, $e \cdot a = a \cdot e = a$,
3. *Existence of inverse.* For any element $a \in G$ there exists an element $b \in G$ so that $a \cdot b = b \cdot a = e$.

B.1 Hue Group.

Following Yang et al. (2024), we identify the elements of the discretized hue group with H_N with elements of the cyclic group C_N . We demonstrate that the set

$$H_N = \left\{ 0, \dots, \frac{2\pi k}{N}, \dots, \frac{2\pi(N-1)}{N} \right\}, \quad (30)$$

with integer k in the range of $0 \leq k < N$, along with the binary operator

$$a \cdot b \mapsto (a + b) \pmod{2\pi}, \quad (31)$$

for $a, b \in H_N$ is a group by showing that it satisfies *associativity* and has *identity* and *inverse* elements.

Associativity. For any hue element $a, b, c \in H_N$, defined as $a = 2\pi k_a/N$, $b = 2\pi k_b/N$, and $c = 2\pi k_c/N$ where k_a, k_b, k_c are integers in the range of $0 \leq k_a, k_b, k_c < N$, we can write

$$(a \cdot b) \cdot c = \left(\left(\frac{2\pi(k_a + k_b)}{N} \right) \pmod{2\pi} + \frac{2\pi k_c}{N} \right) \pmod{2\pi}. \quad (32)$$

By recognizing that modulo operation distributes over addition such that

$$(a + b) \pmod{m} = (a \pmod{m} + b \pmod{m}) \pmod{m}, \quad (33)$$

we can rewrite Equation (32) by distributing such that

$$(a \cdot b) \cdot c = \left(\left(\frac{2\pi k_a}{N} \pmod{2\pi} + \frac{2\pi k_b}{N} \pmod{2\pi} \right) \pmod{2\pi} + \frac{2\pi k_c}{N} \right) \pmod{2\pi}, \quad (34)$$

$$= \left(\left(\frac{2\pi k_a}{N} \pmod{2\pi} + \frac{2\pi k_b}{N} \pmod{2\pi} \right) \pmod{2\pi} \pmod{2\pi} + \frac{2\pi k_c}{N} \pmod{2\pi} \right) \pmod{2\pi}. \quad (35)$$

Leveraging the identity property of modulo

$$(a \pmod{b}) \pmod{b} = (a \pmod{b}), \quad (36)$$

we can rewrite Equation (35) such that

$$(a \cdot b) \cdot c = \left(\left(\frac{2\pi k_a}{N} \pmod{2\pi} + \frac{2\pi k_b}{N} \pmod{2\pi} \right) \pmod{2\pi} + \left(\frac{2\pi k_c}{N} \pmod{2\pi} \right) \pmod{2\pi} \right) \pmod{2\pi}. \quad (37)$$

Using the distributive property, Equation (37) can be written as

$$(a \cdot b) \cdot c = \left(\frac{2\pi k_a}{N} \pmod{2\pi} + \frac{2\pi k_b}{N} \pmod{2\pi} + \frac{2\pi k_c}{N} \pmod{2\pi} \right) \pmod{2\pi}, \quad (38)$$

$$= \left(\left(\frac{2\pi k_a}{N} \pmod{2\pi} \right) \pmod{2\pi} + \left(\frac{2\pi k_b}{N} \pmod{2\pi} + \frac{2\pi k_c}{N} \pmod{2\pi} \right) \pmod{2\pi} \right) \pmod{2\pi}, \quad (39)$$

$$= \left(\frac{2\pi k_a}{N} \pmod{2\pi} + \left(\frac{2\pi k_b}{N} \pmod{2\pi} + \frac{2\pi k_c}{N} \pmod{2\pi} \right) \pmod{2\pi} \right) \pmod{2\pi}, \quad (40)$$

$$= \left(\frac{2\pi k_a}{N} + \left(\frac{2\pi(k_b + k_c)}{N} \right) \pmod{2\pi} \right) \pmod{2\pi}, \quad (41)$$

$$= a \cdot (b \cdot c), \quad (42)$$

which shows that the hue group satisfies associativity.

Identity element. Consider the hue element $0 \in H_N$, then for every element $a = 2\pi k_a/N \in H_N$ we can write

$$a \cdot 0 = \left(\frac{2\pi(k_a + 0)}{N} \right) \pmod{2\pi} = a, \quad (43)$$

and

$$0 \cdot a = \left(\frac{2\pi(0 + k_a)}{N} \right) \pmod{2\pi} = a, \quad (44)$$

which shows that 0 is the identity element of H_N .

Inverse element. For any hue element $a \in H_N$, defined as $a = 2\pi k_a/N$ where k_a is an integer in the range of $0 \leq k_a, k_b, k_c < N$, an inverse element can be written as $a^{-1} = 2\pi(N-k_a)/N$ such that

$$a \cdot a^{-1} = \left(\frac{2\pi(k_a + N - k_a)}{N} \right) \pmod{2\pi} = 2\pi \pmod{2\pi} = 0, \quad (45)$$

and

$$a^{-1} \cdot a = \left(\frac{2\pi(N - k_a + k_a)}{N} \right) \pmod{2\pi} = 2\pi \pmod{2\pi} = 0. \quad (46)$$

As k_a is an integer in the range of $0 \leq k_a < N$, then $N - k_a$ is also in the range of $0 \leq N - k_a < N$, which indicates that $a^{-1} \in H_N$, which shows that a^{-1} is the inverse for all hue elements $a \in H_N$.

B.2 Saturation Group.

We identify the elements of the discretized saturation group with S_N with elements of the cyclic group C_M . We demonstrate that the set

$$S_N = \left\{ 0, \dots, \frac{2\pi k}{M}, \dots, \frac{2\pi(M-1)}{M} \right\}, \quad (47)$$

with integer k in the range of $0 \leq k < M$, along with the binary operator

$$a \cdot b \mapsto (a + b) \pmod{2\pi}, \quad (48)$$

for $a, b \in S_M$. Therefore we can show that S_M is a group analogously to hue in Appendix B.1.

B.3 Luminance Group.

We identify the elements of the discretized luminance group with L_R with elements of the cyclic group C_R . We demonstrate that the set

$$L_N = \left\{ 0, \dots, \frac{2\pi k}{R}, \dots, \frac{2\pi(R-1)}{R} \right\}, \quad (49)$$

with integer k in the range of $0 \leq k < R$, along with the binary operator

$$a \cdot b \mapsto (a + b) \pmod{2\pi}, \quad (50)$$

for $a, b \in L_R$. Therefore we can show that L_R is a group analogously to hue in Appendix B.1.

C Experiments

In this section, we include additional results and discussion for Section 5.

C.1 Degradation of Performance at Large Lifting

To facilitate fair comparison, $\mathbb{T}^3\text{CEN}$ reduces the filter count when increasing total lifting cardinality (the cardinality of the hue, saturation, and luminance added together). When the order of cardinality increases, the reduced filter count may cause a decrease in classification accuracy. We demonstrate this phenomenon on a hue shifted MNIST (LeCun et al., 2002) dataset, where the training images have hue in range of $0^\circ - 120^\circ$ and the testing images have hue in range of $120^\circ - 360^\circ$. We report the classification accuracy at different cardinalities in Figure 8. For instance, the classification error with cardinality 20 is 9.19, while the lowest error of 1.96 is achieved with cardinality 4. We note that the cardinality that produced the peak accuracy matches the analytical with the highest entropy density in Figure 6. We report the corresponding final feature map channel at different cardinalities in Figure 8, where the number of channels drops from 20 to 6.

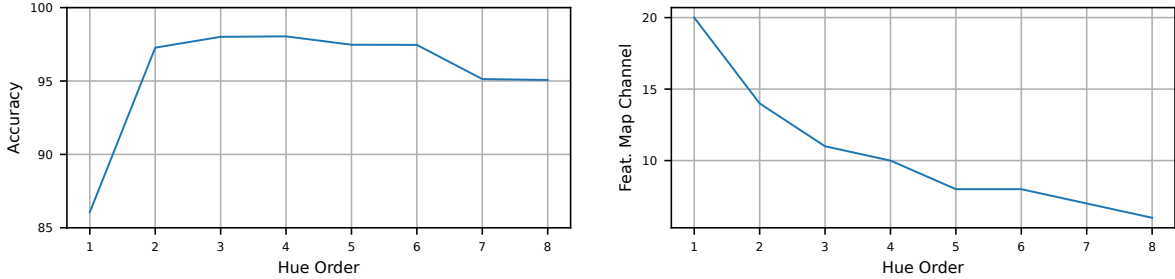


Figure 8: **Degradation of performance with large lifting cardinality.** (Left) We report the classification accuracy with increasing hue cardinality on the hue shift MNIST dataset (LeCun et al., 2002) (for more details see Appendix D.5). With increasing cardinality, the classification accuracy drops. (Right) We report the number of channels in the final feature map with increasing hue cardinality on the Z2CNN architecture (Cohen & Welling, 2016). With increasing cardinality the number of channels drops significantly.

C.2 Saturation Equivariance Error

Following Yang et al. (2024), we define the normalized saturation equivariance error as

$$\Delta_{\varphi_s} = \frac{|f(\varphi_s(s_i, x)) - \phi_s(s_i, f(x))|}{|f(\varphi_s(s_i, x)) + \phi_s(s_i, f(x))|}. \quad (51)$$

We calculate the normalized saturation equivariance error for LCER (Yang et al., 2024) for cardinalities of $M \in \{3, 5, 7, 9, 11, 15\}$ (as LCER use translation for lifting to the saturation group, the resulting cardinality must be odd). The saturation of the shifted input was lowered from the original input image by $1.0/(M-1)$ to match the lifting cardinality in LCER. We again show the equivariance error for LCER in Figure 9, where LCER exhibits significant error averaging 0.445, while $\mathbb{T}^3\text{CEN}$ has average equivariance error of 4.66×10^{-6} (most likely due to computational error rather than architectural).



Figure 9: **Saturation equivariance error.** The normalized saturation equivariance error for $\mathbb{T}^3\text{CEN}$ and LCER is reported. $\mathbb{T}^3\text{CEN}$ has average error of 4.66×10^{-6} while LCER has average error of 0.445.

In Figure 9, we observe that the saturation equivariance error of LCER reduces with increasing cardinality. At each convolution layer after the first, LCER translates the filter orbit and zero-pads the ‘missing’ filter, as described in Equation (6), such that for a group action of s_1 the filter orbit becomes

$$\phi_s(s_1, f) = (f_2, \dots, f_M, \mathbf{0}). \quad (52)$$

The equivariance error is, primarily, a result of the additional zero-padded filter. Intuitively, the effect of the zero-padded filter reduces with increasing cardinality (and therefore filter count). When considered in conjunction with the degradation of performance at large lifting cardinalities (see Appendix C.1 for details), decreasing equivariance error and improving classification accuracy are fundamentally opposing actions for LCER.

C.3 Expanded Results Table

We report the classification accuracies on the vanilla datasets in Table 7.

Table 7: **Generalization to color shift.** Classification error on the Caltech-101, CIFAR-10, CIFAR-100, Oxford-IIT Pets, Stanford Cars, STL-10 datasets are reported. \mathbb{T}^3 CEN performs similarly to CEConv and LCER on the vanilla test datasets.

Network	Original Dataset					
	Caltech 101	CIFAR-10	CIFAR-100	Stanford Cars	Oxford Pets	STL-10
ResNet	32.68 (1.55)	7.86 (1.14)	32.00 (0.63)	25.41 (0.96)	31.52 (2.05)	<u>18.59 (1.65)</u>
ResNet-gray	33.79 (3.09)	8.45 (0.68)	<u>32.04 (0.66)</u>	24.71 (0.93)	30.38 (0.35)	18.71 (1.47)
ResNet-aug	32.90 (0.82)	<u>8.33 (0.44)</u>	32.27 (0.18)	22.38 (1.65)	30.06 (0.52)	17.89 (1.48)
CEConv-3	34.74 (0.83)	8.86 (0.33)	34.95 (0.44)	23.97 (1.56)	31.08 (2.54)	24.29 (1.31)
CEConv-4	33.52 (0.48)	9.28 (0.24)	35.46 (0.35)	24.08 (0.66)	33.70 (1.50)	21.90 (1.64)
LCER-H4	32.23 (1.07)	8.83 (0.64)	34.70 (0.89)	<u>20.38 (1.06)</u>	27.39 (0.68)	20.73 (1.11)
LCER-S3	41.64 (1.40)	9.24 (0.27)	39.33 (0.45)	31.90 (10.03)	36.87 (5.57)	20.71 (1.10)
LCER-H4S3	38.14 (1.07)	10.68 (0.78)	33.27 (0.31)	24.79 (3.87)	<u>29.84 (1.34)</u>	20.53 (0.73)
\mathbb{T}^3 CEN-H4	32.23 (1.07)	8.83 (0.64)	34.70 (0.89)	<u>20.38 (1.06)</u>	27.39 (0.68)	20.73 (1.11)
\mathbb{T}^3 CEN-S4	36.67 (0.65)	9.38 (0.84)	35.08 (0.72)	23.46 (2.95)	35.53 (2.91)	21.50 (1.18)
\mathbb{T}^3 CEN-L4	37.38 (1.18)	9.46 (1.24)	34.74 (0.53)	20.33 (2.20)	41.30 (0.33)	22.77 (0.47)
\mathbb{T}^3 CEN-H4S4	36.58 (0.36)	11.04 (0.90)	40.87 (0.52)	24.98 (0.70)	35.44 (1.03)	21.63 (0.41)
\mathbb{T}^3 CEN-S4L4	37.42 (1.09)	11.18 (0.57)	39.32 (0.27)	25.84 (0.28)	39.94 (4.09)	22.53 (1.06)

D Dataset and Implementation Details

In this section, we include details on the dataset and network implementation for results presented in Section 5.

All experiments were performed over a set of random seeds to evaluate the robustness of \mathbb{T}^3 CEN to initialization. All errors reported for 3D Shapes, Small NORB, CIFAR-10, CIFAR-100, Caltech-101, Oxford Pets, Stanford Cars, and STL-10 are based on three random seeds (1999-2001). The error reported for Camelyon17 were based on five random seeds (1997-2002).

All models were trained on a shared research computing cluster, where each GPU enabled compute node was allocated an Nvidia L40 GPU, 24 core partitions of an Intel Xeon Gold 5320 CPU, and 24GBs of DDR4 3200MHz RDIMMs.

Table 8: **Training hyperparameters.** We report the training hyperparameters on the Caltech-101, CIFAR-10, CIFAR-100, Oxford-IIT Pets, Stanford Cars, STL-10 datasets. All datasets are trained under cross entropy loss. All datasets are training by replacing conventional convolution blocks with \mathbb{T}^3 CEN convolution. The filter count for \mathbb{T}^3 CEN is reduced to match that of the respective vanilla ResNet. Group pooling is performed at the last layer to obtain an invariance representation for classification. LCER and CEConv are training using network parameters provided in Lengyel et al. (2023) and Yang et al. (2024) respectively.

	Caltech 101	CIFAR-10	CIFAR-100	Stanford Cars	Oxford Pets	STL-10
Arch.	ResNet18	ResNet44	ResNet44	ResNet18	ResNet18	ResNet18
Batch Size	16	128	128	16	16	16
Epoch	300	300	300	300	300	300
Optimizer	Adam	SGD	SGD	Adam	Adam	Adam
Learning Rate	10^{-2}	10^{-1}	10^{-1}	10^{-2}	10^{-2}	10^{-2}
Scheduler	N/A	Cos. Anneal.	Cos. Anneal.	N/A	N/A	N/A

We report training hyperparameters for Caltech-101, CIFAR-10, CIFAR-100, Oxford-IIT Pets, Stanford Cars, STL-10 in Table 8. We report training procedure for hue shift 3DShapes, saturation shift 3DShapes, small NORB, and Camelyon17 in their individual sections.

D.1 Hue Shift 3D Shapes

We evaluate the hue-equivariance performance of $\mathbb{T}^3\text{CEN}$ on the hue shift 3D Shapes (Krause et al., 2013). The train set and in-distribution test set (*A*) consists of images where the floor, background, and object all have warm hue (indexed by 0-4 in the original 3D Shapes dataset); the first out-of-distribution test set (*B*) consists of images where the floor, background, and object all have cold hue (indexed by 5-9 in the original 3D Shapes dataset); and the second out-of-distribution test set (*C*) consists of images where the floor and background have warm hue and the object has cold hue. Example images from all three subsets are shown in Figure 10.

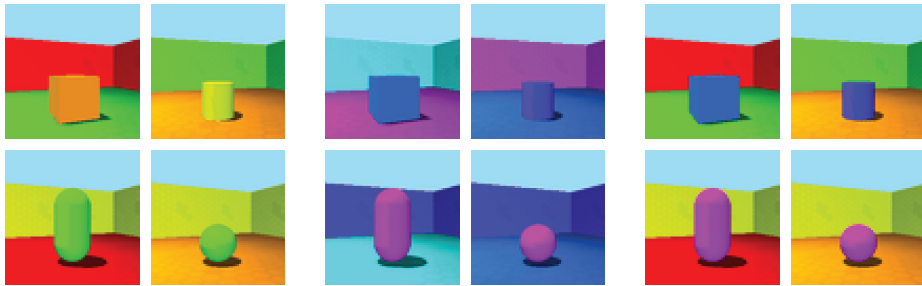


Figure 10: **Hue shift 3D Shapes dataset.** (Left) The train set and in-distribution test set *A*, where the floor, background, and object all have warm hues (colors 0-4); (Middle) The first out-of-distribution test set *B*, where the floor, background, and object all have cold hues (colors 5-9); (Right) The second out-of-distribution test set *C*, where the floor and background have warm hues and the object has cold hues.

We compare the classification accuracy of hue-equivariant $\mathbb{T}^3\text{CEN}$ with ResNet44 (He et al., 2016), CEConv (Lengyel et al., 2023), and hue-equivariant LCER (Yang et al., 2024). $\mathbb{T}^3\text{CEN}$ has the same architectural backbone as ResNet44, but with a reduced filter count to ensure similar number of network parameters. We perform group pooling at the last layer of $\mathbb{T}^3\text{CEN}$ to obtain a hue-invariant representation for classification. We optimized $\mathbb{T}^3\text{CEN}$ under cross-entropy loss using Adam (Kingma, 2014) with learning rate of 10^{-4} for 10,000 iterations with a batch size of 128.

D.2 Saturation Shift 3D Shapes

We evaluate the saturation-equivariance performance of $\mathbb{T}^3\text{CEN}$ on the saturation shift 3D Shapes (Krause et al., 2013). The train set and in-distribution test set (*A*) consists of images with the original saturation; the first out-of-distribution test set (*B*) consists of images with regular saturation shifts of multiples of 0.125; and the second out-of-distribution test set (*C*) consists of images with saturation shifts of random values. Example images from all three subsets are shown in Figure 11.

We compare the classification accuracy of saturation-equivariant $\mathbb{T}^3\text{CEN}$ with ResNet44 (He et al., 2016) and saturation-equivariant LCER (Yang et al., 2024). $\mathbb{T}^3\text{CEN}$ has the same architectural backbone as ResNet44, but with a reduced filter count to ensure similar number of network parameters. We perform group pooling at the last layer of $\mathbb{T}^3\text{CEN}$ to obtain a saturation-invariant representation for classification. We optimized $\mathbb{T}^3\text{CEN}$ under cross-entropy loss using Adam (Kingma, 2014) with learning rate of 10^{-4} for 10,000 iterations with a batch size of 128.

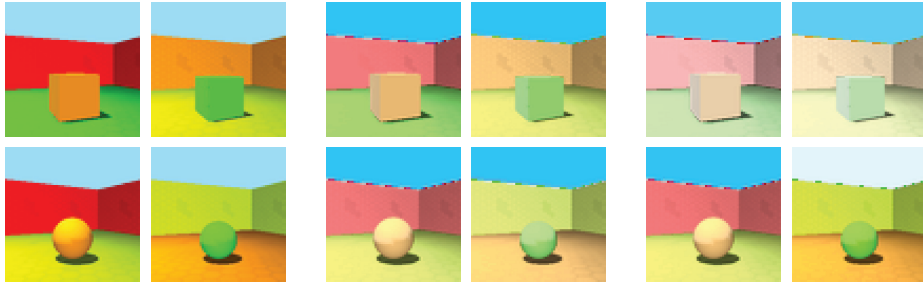


Figure 11: **Saturation shift 3D Shapes dataset.** **(Left)** The train set and in-distribution test set A with original saturation values; **(Middle)** The first out-of-distribution test set B with regular saturation shifts of multiples of 0.125; **(Right)** The second out-of-distribution test set C with saturation shifts of random values.

D.3 HSL Shift 3D Shapes

We evaluate the HSL-equivariance performance of T^3CEN on the HSL shift 3D Shapes (Krause et al., 2013). The train set and in-distribution test set (A) consists of images with the original hue, saturation, and luminance; the test set consists of images with random shifts in HSL.

We compare the classification accuracy of HSL-equivariant T^3CEN with ResNet44 (He et al., 2016). T^3CEN has the same architectural backbone as ResNet44, but with a reduced filter count to ensure similar number of network parameters. We perform group pooling at the last layer of T^3CEN to obtain a HSL-invariant representation for classification. We optimized T^3CEN under cross-entropy loss using Adam (Kingma, 2014) with learning rate of 10^{-4} for 10,000 iterations with a batch size of 128.

D.4 Small NORB

We evaluate the performance of T^3CEN in the presence of lighting shifts on the small NORB (LeCun et al., 2004) dataset, which consists of 48.6k 96×96 resolution grayscale images rendered under 6 lighting conditions, 9 elevations, and 18 azimuths. For ease of processing (as the original dataset was stored using MATLAB files), we use the pre-processed dataset given in <https://huggingface.co/datasets/Ramos-Ramos/smallnorb>. The train set and in-distribution test set (A) consists of images with medium lighting conditions (2-3 as defined in LeCun et al. (2004)); the first out-of-distribution test set (B) consists of images with low lighting conditions (0-1 as defined in LeCun et al. (2004)); and the second out-of-distribution test set (C) consists of images with high lighting conditions (4-5 as defined in LeCun et al. (2004)). Example images from all three subsets are shown in Figure 12.

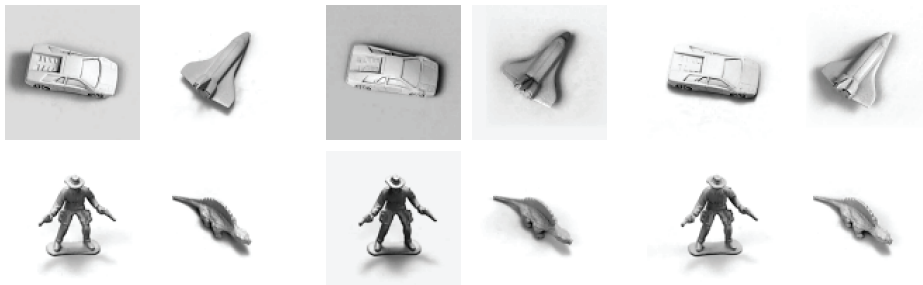


Figure 12: **Small NORB dataset.** **(Left)** The train set and in-distribution test set A with medium lighting conditions; **(Middle)** The first out-of-distribution test set B with low lighting conditions; **(Right)** The second out-of-distribution test set C with high lighting conditions.

We compare the classification accuracy of luminance-equivariant T^3CEN with ResNet18 (He et al., 2016) and luminance-equivariant LCER (Yang et al., 2024). T^3CEN has the same architectural backbone as ResNet18, but with

a reduced filter count to ensure similar number of network parameters. We perform group pooling at the last layer of T^3CEN to obtain a luminance-invariant representation for classification. We optimized T^3CEN under cross-entropy loss using Adam (Kingma, 2014) with learning rate of 10^{-2} for 300 epochs with a batch size of 16.

D.5 Hue Shift MNIST

We evaluate the performance of T^3CEN with at different cardinalities using the hue shift MNIST (LeCun et al., 2002) dataset. The train set includes hue in the range of $0^\circ - 120^\circ$ and the test set includes hue in the range of $120^\circ - 360^\circ$. Example images are shown in Figure

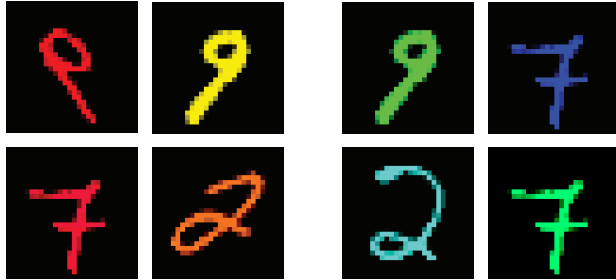


Figure 13: **Hue shift MNIST dataset.** (Left) The train set hue in range of $0^\circ - 120^\circ$ and (Right) the test set hue in range of $120^\circ - 360^\circ$.

We compare the classification accuracy of T^3CEN at with hue lifted to different cardinalities. T^3CEN has the same architectural backbone as Z2CNN (Cohen & Welling, 2016), but with a reduced filter count to ensure similar number of network parameters. We perform group pooling at the last layer of T^3CEN to obtain a hue-invariant representation for classification. We optimized T^3CEN under cross-entropy loss using SGD with learning rate of 10^{-3} for 5 epochs with a batch size of 128.

D.6 Camelyon17

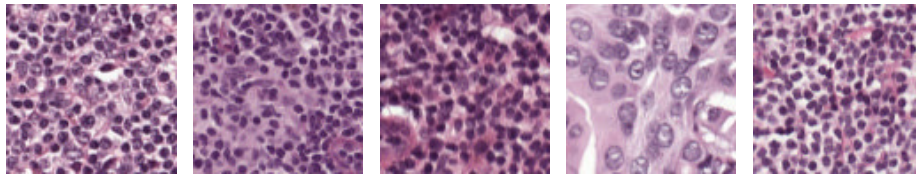


Figure 14: **Camelyon17 dataset.** (Left-Right) Example images of cells from hospital 1-5.

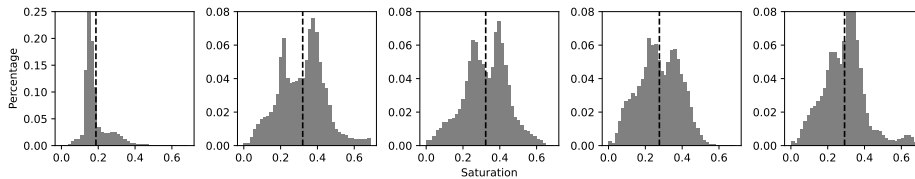


Figure 15: **Camelyon17 dataset saturation distribution.** (Left-Right) Saturation distribution of images from hospital 1-5.

We evaluate the performance of T^3CEN on medical imaging on the Camelyon17 (Bandi et al., 2018) dataset. The dataset consists of Whole-Slide Images (WSI) of Hematoxylin and Eosin (H&E) stained lymph node sections. For

each patient, five slides are provided. A total of 100 patient slide imaging is released, with 50 for training and 50 for testing. The training dataset consists of all imaged from hospital 1, 2, and 3, the validation dataset consists of all images from hospital 4, and the testing dataset consists of all images from hospital 5. Example cell images from all five hospitals are shown in Figure 14. We show the distribution of image saturation values in Figure 15.

We compare the classification accuracy of $\mathbb{T}^3\text{CEN}$ with ResNet50 (He et al., 2016), CEConv (Lengyel et al., 2023), and LCER (Yang et al., 2024). $\mathbb{T}^3\text{CEN}$ has the same architectural backbone as ResNet50, but with a reduced filter count to ensure similar number of network parameters. We perform group pooling at the last layer of $\mathbb{T}^3\text{CEN}$ to obtain a invariant representation for classification. We optimized $\mathbb{T}^3\text{CEN}$ under cross-entropy loss using Adam (Kingma, 2014) with learning rate of 10^{-2} . We trained $\mathbb{T}^3\text{CEN}$ for 10,000 iterations with a batch size of 32.